Article

Neuron

Projection-Specific Dynamic Regulation of Inhibition in Amygdala Micro-Circuits

Highlights

- IL- and PL-projecting BLA PNs receive uniform inhibition from $CB1R^{+}$ CCK_{L} interneurons
- CCK_{L}-PN_{IL} synapses are more susceptible to activity-dependent suppression
- PN_{IL} display a higher abundance of the endocannabinoid-synthesizing enzyme DGLα
- Differential DGLα abundance in PN_{IL} and PN_{PL} is stable after fear conditioning

Authors

Elisabeth Vogel, Sabine Krabbe, Jan Gründemann, Jaclyn I. Wamsteeker Cusulin, Andreas Lüthi

Correspondence

andreas.luthi@fmi.ch

In Brief

Cannabinoid receptor-expressing CCK interneurons are key regulators of neuronal circuits. Here, Vogel, Krabbe et al. report a dichotomic regulation of CCK interneuron synaptic transmission onto distinct basolateral amygdala output neurons via subpopulation-specific retrograde CB1R-mediated endocannabinoid signaling.

Vogel et al., 2016, Neuron *91*, 644–651
August 3, 2016
http://dx.doi.org/10.1016/j.neuron.2016.06.036

CellPress

CellPress

Neuron
Article

Projection-Specific Dynamic Regulation of Inhibition in Amygdala Micro-Circuits

Elisabeth Vogel,[1,2,4] Sabine Krabbe,[1,4] Jan Gründemann,[1] Jaclyn I. Wamsteeker Cusulin,[1,3] and Andreas Lüthi[1,2,*]
[1]Friedrich Miescher Institute for Biomedical Research, 4058 Basel, Switzerland
[2]University of Basel, 4000 Basel, Switzerland
[3]Present address: Roche Pharmaceutical Research and Early Development, Neuroscience Ophthalmology and Rare Diseases Discovery & Translational Area, Roche Innovation Center Basel, F. Hoffmann-La Roche, 4070 Basel, Switzerland
[4]Co-first author
*Correspondence: andreas.luthi@fmi.ch
http://dx.doi.org/10.1016/j.neuron.2016.06.036

SUMMARY

Cannabinoid receptor type 1 (CB1R)-expressing CCK interneurons are key regulators of cortical circuits. Here we report that retrograde endocannabinoid signaling and CB1R-mediated regulation of inhibitory synaptic transmission onto basal amygdala principal neurons strongly depend on principal neuron projection target. Projection-specific asymmetries in the regulation of local inhibitory micro-circuits may contribute to the selective activation of distinct amygdala output pathways during behavioral changes.

INTRODUCTION

Principal neuron (PN) activity and function is defined by their long-range projection targets (Brown and Hestrin, 2009; Le Bé and Markram, 2006). PNs with different presynaptic inputs, functional roles, and axonal target regions can be spatially intermingled (Brown and Hestrin, 2009; Le Bé and Markram, 2006; Senn et al., 2014). However, inhibitory control within local micro-circuits is typically broad (Bock et al., 2011; Harris and Mrsic-Flogel, 2013; Hofer et al., 2011; Liu et al., 2010; Wehr and Zador, 2003), and it is not well understood how neighboring PNs with opposing functions are selectively regulated by local inhibitory neurons. Recent reports indicate that cholecystokinin-positive basket cells (CCK BCs), GABAergic interneurons (INs) expressing the cannabinoid receptor type 1 (CB1R), can mediate target-specific inhibition of PNs, both at the cellular (Varga et al., 2010) and subcellular levels (Dudok et al., 2015). CCK BCs might thus play a general role in the selective inhibition of distinct long-range, circuit-specific PNs.

From the basal nucleus of the amygdala (BA), distinct populations of PNs project to the prelimbic (PL) or infralimbic (IL) subdivisions of the medial prefrontal cortex (mPFC) (Hoover and Vertes, 2007; Senn et al., 2014). PL-projecting BA PNs (PN_{PL}s) are activated in vivo during states of high fear, whereas IL-projecting BA PNs (PN_{IL}s) increase their activity in low fear states, such as with acquisition of fear extinction (Senn et al., 2014), which is consistent with the function of the targeted mPFC subdivisions (Burgos-Robles et al., 2009; Quirk and Mueller, 2008; Sierra-Mercado et al., 2011). Recent data indicate that the switch between high fear and low fear states is mediated by a shift of activity in these two amygdala output pathways (Senn et al., 2014). However, the underlying circuit mechanisms mediating such a shift remain unknown.

CB1R-expressing CCK BCs have been suggested to play an important role in mood disorders and in fear extinction (Freund, 2003; Marsicano et al., 2002). In the amygdala, large somata CCK BCs (CCK_L) represent the sole amygdala IN type expressing CB1Rs and form a population distinct from calretinin and/or vasoactive intestinal peptide (VIP)-expressing small CCK INs (CCK_S) (Katona et al., 2001; Mascagni and McDonald, 2003). Given the importance of CB1Rs and endocannabinoids for fear extinction (Marsicano et al., 2002), and the opposing behavioral functions of projections from the BA to PL or IL during fear extinction (Senn et al., 2014), we tested the hypothesis that local BA CCK_Ls differentially inhibit defined subpopulations of BA PNs to balance the activity of functionally distinct BA→mPFC output pathways.

RESULTS

Uniform Unitary Connectivity and Inhibitory Synaptic Strength between CCK_L INs and IL- or PL-Projecting PNs

To probe the functional organization of CCK_L-mediated inhibition onto defined populations of PNs, we performed paired whole-cell patch-clamp recordings of CCK_Ls and retrogradely labeled projection neurons (n = 225 pairs) in acute brain slices of CCK-IN-GFP mice (Figure 1). Selective GFP expression in CCK INs was obtained via an intersectional approach, using CCK-IRES-Cre::Dlx-Flp::RCE:dual reporter mice (Miyoshi et al., 2010). GFP^+ neurons with somatic size similar to mPFC-projecting neurons were considered as CCK_Ls (median [25^{th}/75^{th} percentile]; PN_{mPFC}: 918.8 [763.4/1,063] μm^2, n = 122 cells, N = 3 mice; CCK_L: 848.0 [754.8/977.9] μm^2, n = 103, N = 3; Figures S1A–S1D) and targeted for subsequent experiments. Immunohistochemical analysis revealed that the majority of GFP^+ CCK_Ls were immunopositive for CCK (mean ± SEM; 89.0% ± 1.9%, N = 4, Figures S1E and S1F).

To record from identified PN_{IL}s and PN_{PL}s in ex vivo brain slices, we stereotaxically injected fluorescent latex retrobeads into IL or PL (Figure S2) prior to patch-clamp experiments. Paired recordings from GFP^+ CCK_Ls and $bead^+$ PNs revealed robust,

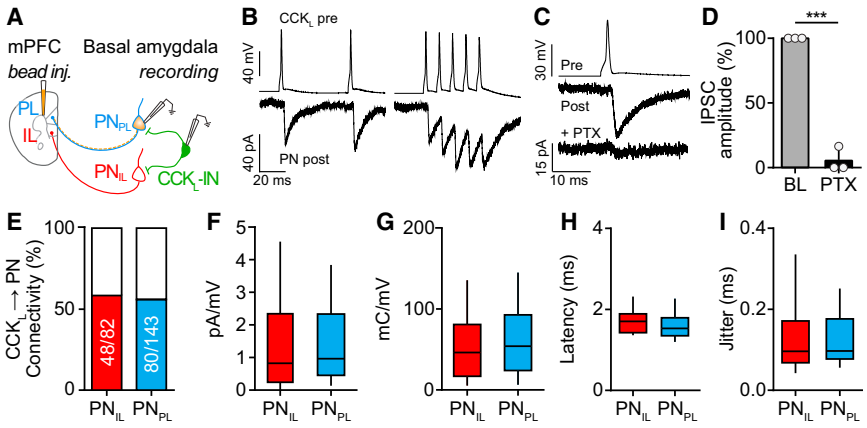

Figure 1. Uniform Connectivity and Strength of CCK_L Synapses onto IL- and PL-Projecting Principal Neurons in Basal Amygdala

(A) Experimental design.

(B) Example traces; connectivity between GFP-positive CCK_Ls and retrobead-labeled PNs was assessed by eliciting two action potentials (APs) in the presynaptic cell (inter-spike interval: 50 ms) followed by a burst of five APs (100 Hz, above). Resulting inhibitory postsynaptic currents were recorded in voltage clamp (below).

(C and D) $CCK_L \rightarrow PN$ synaptic transmission (baseline [BL]) is blocked by GABA-A receptor antagonist picrotoxin (PTX; 100 μM; n = 3 cells, N = 3 mice, paired t test $p < 0.0001$; data represent mean ± SEM).

(E) Connection probability for $CCK_L \rightarrow PN$ pairs is similar between PNs with different mPFC projection targets ($CCK_L \rightarrow PN_{IL}$: 58.5%, n = 82 tested pairs, N = 34; $CCK_L \rightarrow PN_{PL}$: 55.9%, n = 143, N = 51, Fisher's exact test $p > 0.05$).

(F) Synaptic conductance of $CCK_L \rightarrow PN$ unitary IPSCs. Slope was calculated from IPSC amplitude of three different holding levels (−50, −60, and −70 mV; $CCK_L \rightarrow PN_{IL}$: n = 40, N = 21; $CCK_L \rightarrow PN_{PL}$: n = 67, N = 32; t test $p > 0.05$).

(G) Synaptic charge transfer resulting from a 100 Hz presynaptic burst. Slope was calculated from IPSC charge transfer (50 ms window after IPSC onset) at three different holding potentials (−50, −60, and −70 mV; $CCK_L \rightarrow PN_{IL}$: n = 41, N = 21; $CCK_L \rightarrow PN_{PL}$: n = 68, N = 32; MWU test $p > 0.05$).

(H) IPSC latency did not differ between cell types (calculated from presynaptic AP threshold to IPSC onset; $CCK_L \rightarrow PN_{IL}$: n = 18, N = 14; $CCK_L \rightarrow PN_{PL}$: n = 27, N = 20; MWU test $p > 0.05$).

(I) Jitter was calculated as the SD from IPSC latency and does not differ between groups ($CCK_L \rightarrow PN_{IL}$: n = 18, N = 14; $CCK_L \rightarrow PN_{PL}$: n = 27, N = 20; MWU test $p > 0.05$). Data (F–I) are presented as median with $25^{th}/75^{th}$ percentiles (box) and 10^{th} to 90^{th} percentiles (whiskers); ***$p < 0.001$.

picrotoxin-sensitive GABAergic synaptic transmission from CCK_Ls to both IL- and PL-projecting PNs (Figures 1A–1D) with a success rate of 96.3% for $CCK_L \rightarrow PN_{IL}$ and 98.0% for $CCK_L \rightarrow PN_{PL}$ synapses. Connection probability was similar for both PN populations ($CCK_L \rightarrow PN_{IL}$: 58.5%, n = 82 tested pairs, N = 34; $CCK_L \rightarrow PN_{PL}$: 55.9%, n = 143, N = 51; Fisher's exact test $p > 0.05$; Figure 1E). Synaptic conductance did not significantly differ between $CCK_L \rightarrow PN_{IL}$ and $CCK_L \rightarrow PN_{PL}$ pairs in response to single presynaptic action potentials (APs) or 50 ms, 100 Hz AP bursts (Figures 1F and 1G). Interestingly, in contrast to hippocampal CCK BCs (Hefft and Jonas, 2005), inhibitory postsynaptic current (IPSC) latency at $CCK_L \rightarrow PN_{IL}/PN_{PL}$ synapses was short ($CCK_L \rightarrow PN_{IL}$: 2.13 (1.78/2.36) ms, n = 18, N = 14; $CCK_L \rightarrow PN_{PL}$: 1.91 (1.69/2.24) ms, n = 27, N = 20; Mann-Whitney U [MWU] test $p > 0.05$) with low jitter ($CCK_L \rightarrow PN_{IL}$: 0.10 (0.07/0.17) ms, n = 18, N = 14; $CCK_L \rightarrow PN_{PL}$: 0.10 (0.08/0.18) ms, n = 27, N = 20; MWU test $p > 0.05$) but did not differ between groups (Figures 1H and 1I). Comprehensive analysis of cellular properties revealed significant differences between large and small CCKs but not between CCK_Ls targeting IL- or PL-projecting PNs (Table S1). Together, these results indicate that, on the level of unitary synaptic connectivity and strength, distinct subpopulations of mPFC-projecting BA PNs receive uniform, reliable, and rapid inhibition by CCK_Ls.

Projection-Target-Dependent Asymmetric Expression of Retrograde Endocannabinoid Signaling at $CCK_L \rightarrow PN$ Synapses

Given the evidence for CB1R-dependent mechanisms in CCK BC-mediated micro-circuit regulation (Armstrong and Soltesz, 2012; Freund, 2003; Trouche et al., 2013) and amygdala-driven fear extinction (Marsicano et al., 2002), we assessed depolarization-induced suppression of inhibition (DSI), an endocannabinoid-dependent form of short-term plasticity (Ohno-Shosaku et al., 2001; Wilson et al., 2001; Wilson and Nicoll, 2001). To induce DSI, we depolarized postsynaptic PNs to 0 mV for 5 s to mimic strong postsynaptic activity (Figure 2A) (Ohno-Shosaku et al., 2001; Wilson and Nicoll, 2001). At many CB1R-expressing IN synapses, this acts as a trigger for postsynaptic endocannabinoid synthesis and release, causing a transient CB1R-mediated suppression of presynaptic release probability (Galarreta et al., 2004; Wilson and Nicoll, 2002). In the BA, an immediate and robust decrease of IPSC amplitude following postsynaptic depolarization was recorded, which was completely prevented by application of the CB1R antagonist AM251 (Figure 2B). While such DSI was observed at all $CCK_L \rightarrow PN_{IL}$ synapses, $CCK_L \rightarrow PN_{PL}$ synapses were less frequently inhibited (Figures 2C and 2D). On average, DSI magnitude significantly differed between PNs in a target-specific manner ($CCK_L \rightarrow PN_{IL}$: 99.6 (89.1/100)% DSI, n = 20, N = 14; $CCK_L \rightarrow PN_{PL}$: 65.0 (19.5/96.9)%, n = 32, N = 21; MWU test $p < 0.001$; Figure 2E). To investigate whether a more physiological spike pattern could elicit DSI, we additionally tested postsynaptic high-frequency firing activity (Poisson-distributed spike trains, mean frequency: 100 Hz, 5 s) to induce DSI at $CCK_L \rightarrow PN_{IL}$ synapses. Indeed, we found a significant reduction of CCK_L-IPSCs in four out of five $CCK_L \rightarrow PN_{IL}$ pairs (69.8% ± 13.3% DSI, n = 4, N = 4; paired t test $p < 0.05$; Figure S3).

Short-Term Plasticity of $CCK_L \rightarrow PN_{PL/IL}$ Synapses

Next, given the asymmetric expression of DSI at $CCK_L \rightarrow PN_{IL/PL}$ synapses, we investigated whether other forms of short-term plasticity might also differ in a projection target-specific manner. We found no difference in paired-pulse ratio between both

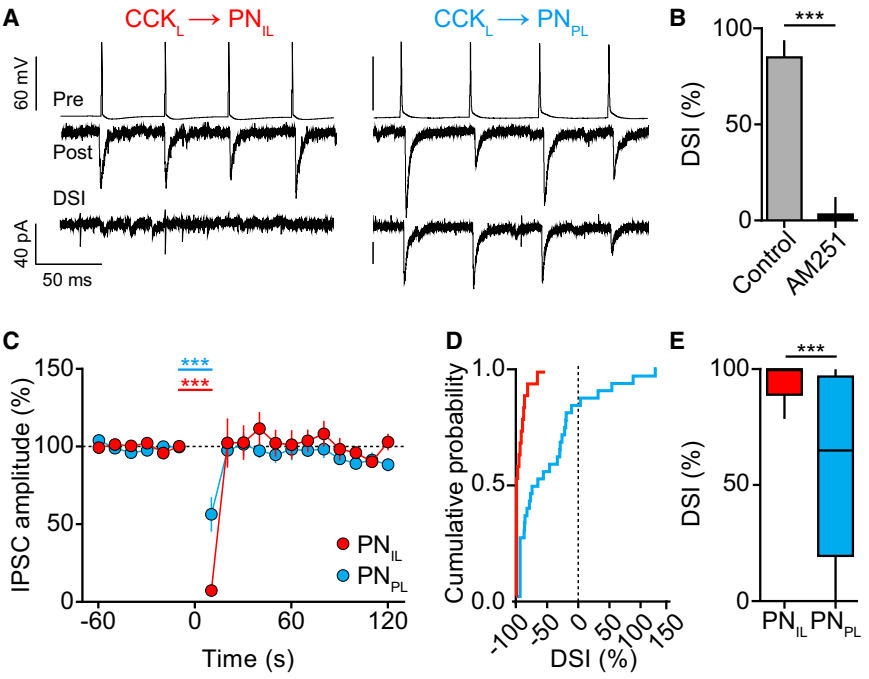

Figure 2. Projection-Target-Dependent Asymmetric Expression of Retrograde Endocannabinoid Signaling at CCK$_L$→PN Synapses

(A) Example traces showing depolarization-induced suppression of inhibition (DSI) at CCK$_L$→PN$_{IL}$ and CCK$_L$→PN$_{PL}$ synapses. IPSCs were evoked by trains of eight APs at 20 Hz in presynaptic CCK$_L$s every 10 s. To induce DSI, we depolarized PNs to 0 mV for 5 s.

(B) DSI at CCK$_L$→PN synapses is abolished by CB1R antagonist AM251 (10 μM; n = 3, N = 3, t test $p < 0.001$.

(C) Time course of IPSC suppression following DSI induction at CCK$_L$→PN synapses. Postsynaptic IPSC amplitudes from one train are averaged to form each data point (CCK$_L$→PN$_{IL}$: n = 20, N = 14, Wilcoxon matched-pairs signed-rank test $p < 0.0001$ compared to baseline recording; CCK$_L$→PN$_{PL}$: n = 32, N = 21, $p < 0.001$).

(D) Distribution of DSI magnitudes for PN projection classes (CCK$_L$→PN$_{IL}$: n = 20, N = 14; CCK$_L$→PN$_{PL}$: n = 32, N = 21; Kolmogorov-Smirnov test $p < 0.01$).

(E) Circuit-specific differences in DSI expression. DSI is presented as percent decrease in mean IPSC amplitude of the first train following PN depolarization compared with preceding 60 s baseline recording (CCK$_L$→PN$_{IL}$: n = 20, N = 14; CCK$_L$→PN$_{PL}$: n = 32, N = 21; MWU test $p < 0.001$). Data are presented as mean ± SEM or median (E) with 25th/75th percentiles (box) and 10th to 90th percentiles (whiskers); ***$p < 0.001$.

populations (two presynaptic action potentials, frequency: 20 Hz, Figure 3A). However, upon delivery of brief presynaptic high-frequency bursts (100 Hz, 5 pulses), CCK$_L$→PN$_{IL}$ synapses exhibited stronger depression compared to CCK$_L$→PN$_{PL}$ synapses (Figure 3B). Thus, in contrast to the uniform synaptic connectivity and strength, dynamic short-term regulation of CCK$_L$ synapses depends on the identity of the postsynaptic target cell with CCK$_L$→PN$_{IL}$ synapses being more susceptible to activity-dependent suppression.

Projection-Specific Expression of Endocannabinoid-Synthesizing Enzyme DGLα

Next, we examined whether pre- or postsynaptic factors underlie the target specificity of DSI. To explore whether differential CB1R expression or tonic CB1R activation could account for alterations in DSI, we applied the CB1R agonist WIN55,212-2 (5 μM) during paired recordings. We observed that CCK$_L$-IPSCs onto PN$_{IL}$s and PN$_{PL}$s were depressed with similar effect in magnitude and time course (Figure 3C). No correlation of suppression by WIN with DSI magnitude was observed (Figure 3D). Additionally, we tested whether CCK$_L$ synapses are tonically suppressed by endocannabinoids. However, application of AM251 (10 μM) had no effect on IPSC amplitude for either postsynaptic target (CCK$_L$→PN$_{IL}$ 12.2% ± 19.6%, n = 5, N = 5; CCK$_L$→PN$_{PL}$ 0.5% ± 22.1%, n = 4, N = 4). Together, these results suggest that lower DSI levels in PL-projecting cells cannot be explained by a presynaptic mechanism.

To address whether postsynaptic differences in IL- versus PL-projecting PNs could account for altered endocannabinoid signaling, we examined the subcellular abundance of the endocannabinoid synthesis (diacylglycerol lipase α [DGLα]) and degradation (monoacylglycerol lipase [MGL]) enzymes for 2-arachidonylglycerol, the main endocannabinoid contributing to DSI at central synapses (Hashimotodani et al., 2008; Tanimura et al., 2010). Using immunohistochemistry, we first quantified co-expression of the vesicular GABA transporter (VGAT) in CB1R$^+$ bouton-like appositions on the somatic surface of Cholera-toxin-B labeled IL- and PL-projecting PNs (Figures S4A and S4B). 98.2% ± 0.5% of CB1R$^+$ varicosities were also immunopositive for VGAT, indicating that the vast majority of somatic CB1R$^+$ contacts reflect synapses from GABAergic neurons. Consistent with the electrophysiological results, no difference in the number of double-labeled VGAT$^+$ and CB1R$^+$ bouton-like appositions could be detected between IL- and PL-projecting PNs (Figures S4A–S4C and Tables S2 and S3). Next, we quantified DGLα$^+$ puncta closely apposed to CB1R$^+$ varicosities at the cell surface of postsynaptic IL- or PL-projecting PNs. Blinded analysis revealed a circa 50% higher number of DGLα$^+$ puncta in IL-projecting cells (PN$_{IL}$: 48.0 (38.3/55.8) spots per soma, n = 64, N = 3; PN$_{PL}$: 32.0 (25.0/39.0), n = 88, N = 3; MWU test, $p < 0.0001$; Figures 4A–4C). Similar results were obtained in triple-labeled sections in which somatic DGLα$^+$ appositions to double-labeled VGAT$^+$/CB1R$^+$ boutons were quantified (Figures S4D–S4F). To confirm the postsynaptic location of DGLα, we performed co-immunolabeling of DGLα with gephyrin, a postsynaptic structural protein at GABAergic synapses (Sassoè-Pognetto et al., 2000). Again, a significantly higher number of DGLα$^+$ spots were co-localized with gephyrin in IL-projecting PNs (Figures S4G–S4I). Further, the higher numbers of DGLα$^+$ puncta in PN$_{IL}$s could not be accounted to a difference in PN

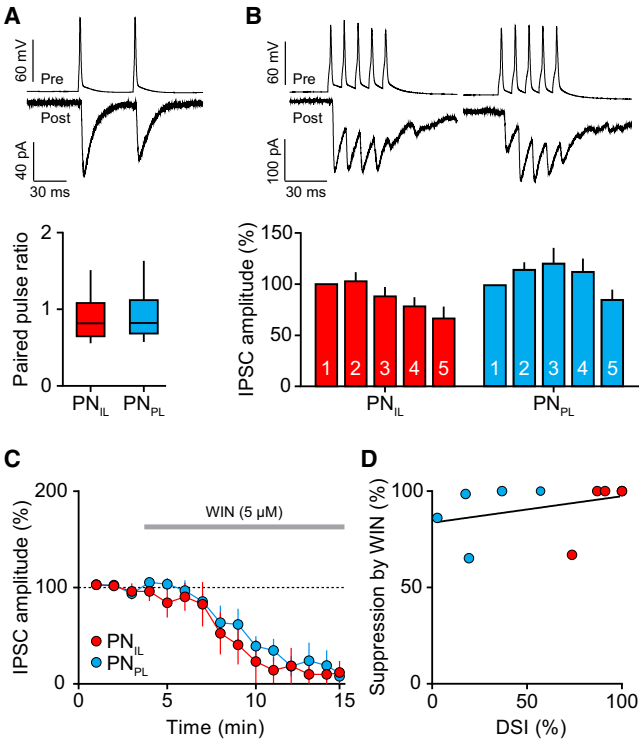

Figure 3. Short-Term Plasticity of $CCK_L \rightarrow PN_{PL/IL}$ Synapses

(A) Example traces (above) and quantification (below) of paired-pulse ratio; CCK_Ls were driven to fire action potentials (AP) with an inter-spike interval of 50 ms. Paired-pulse ratio (second IPSC amplitude over first IPSC amplitude) for cells recorded from each postsynaptic target group did not significantly differ ($CCK_L \rightarrow PN_{IL}$: n = 43, N = 24; $CCK_L \rightarrow PN_{PL}$: n = 66, N = 34; MWU test $p > 0.05$.

(B) $CCK_L \rightarrow PN_{PL/IL}$ IPSC dynamics in response to 100 Hz AP bursts; amplitude of the first IPSC was measured from baseline, IPSCs 2–5 were measured from peak of decay of preceding IPSC to maximum amplitude and normalized to IPSC 1. $CCK_L \rightarrow PN_{IL}$ synapses exhibit IPSC amplitude depression compared with $CCK_L \rightarrow PN_{PL}$ synapses ($CCK_L \rightarrow PN_{IL}$: n = 35, N = 22; $CCK_L \rightarrow PN_{PL}$: n = 58, N = 33; two-way ANOVA $F_{4,364} = 5.096$, $p < 0.001$, post hoc Bonferroni multiple comparisons: IL_1 versus IL_5 $p < 0.05$).

(C) Suppression of synaptic transmission by application of CB1R agonist WIN55,212-2 (WIN; 5 μM; $CCK_L \rightarrow PN_{IL}$: n = 5, N = 5; $CCK_L \rightarrow PN_{PL}$: n = 5, N = 5). No difference between synapses onto PN_{IL}s and PN_{PL}s could be detected (two-way ANOVA $F_{1,8} = 0.7201$, $p > 0.05$).

(D) No significant correlation between DSI magnitude and WIN-induced reduction in IPSC amplitude was observed (linear regression, $p > 0.05$). Data are presented as median (A) with $25^{th}/75^{th}$ percentiles (box) and 10^{th} to 90^{th} percentiles (whiskers) or mean ± SEM (B and C).

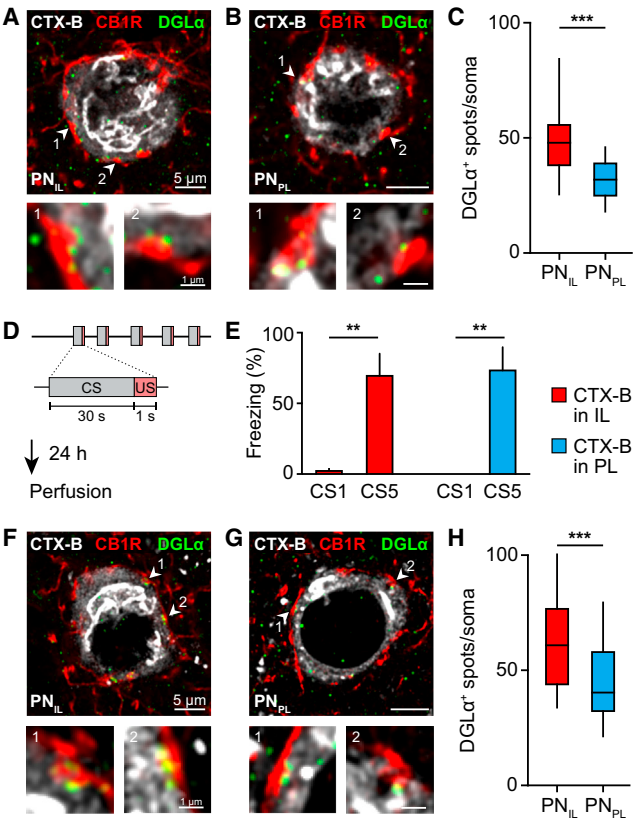

Figure 4. Projection-Specific Expression of Endocannabinoid Synthesizing Enzyme DGLα

(A and B) Example images illustrating DGLα expression in BA PN_{IL}s (A) and PN_{PL}s (B); a single focal plane is shown. Smaller panels depict higher-magnification images of somatic appositions indicated with arrows. Gray: CTX-B, red: CB1R, green: DGLα.

(C) A significantly greater number of $DGL\alpha^+$ puncta in apposition to $CB1R^+$ varicosities were detected in PN_{IL}s (PN_{IL}: n = 64, N = 3; PN_{PL}: n = 88, N = 3; MWU test $p < 0.0001$).

(D) Mice were subjected to an auditory fear-conditioning paradigm with five CS-US pairings and sacrificed for immunohistochemical analysis 24 hr later.

(E) Freezing to CS5 is significantly increased compared to CS1 for both IL- and PL-injected mice but does not differ between both groups (two-way ANOVA $F_{1,10} = 36.30$, $p < 0.001$; post hoc Bonferroni multiple comparisons: $CS1_{IL}$ versus $CS5_{IL}$ $p < 0.01$, N = 4; $CS1_{PL}$ versus $CS5_{PL}$ $p < 0.01$, N = 3).

(F and G) Example images illustrating DGLα expression in PN_{IL}s (F) and PN_{PL}s (G) in the BA 24 hr after auditory fear conditioning; a single focal plane is shown. Smaller panels show higher-magnification images of somatic appositions indicated with arrows. Gray: CTX-B, red: CB1R, green: DGLα.

(H) PN_{IL}s display a significantly higher number of $DGL\alpha^+$ puncta in apposition to $CB1R^+$ varicosities (PN_{IL}: n = 56, N = 4; PN_{PL}: n = 44, N = 3; MWU test $p < 0.001$). Immunohistochemical quantification data are presented as median with $25^{th}/75^{th}$ percentiles (box) and 10^{th} to 90^{th} percentiles (whiskers); freezing data are presented as mean ± SEM; $^{**}p < 0.01$, $^{***}p < 0.001$.

cell size, as both IL- and PL-projecting PNs exhibited similar somatic surface areas (PN_{IL}: 1,045 ± 14 μm^2, n = 41, N = 4; PN_{PL}: 1,036 ± 23 μm^2, n = 42, N = 3; t test $p > 0.05$). In contrast to higher postsynaptic DGLα abundance in PN_{IL}s, preliminary data show no difference in presynaptic MGL expression in perisomatic $CB1R^+$ terminals surrounding IL- and PL-projecting PNs (Figures S4J–S4L).

Since the balance of activity between IL- and PL-projecting pathways was previously described to be important for fear extinction learning (Senn et al., 2014), we investigated whether the difference in DGLα abundance would change after fear learning. We submitted mice injected with Choleratoxin-B to either of the two prefrontal projection targets to an auditory fear conditioning paradigm (Figure 4D). All mice acquired a strong fear memory during the conditioning session (Figure 4E) and were sacrificed 24 hr later for immunohistochemical analysis. Quantification of $DGL\alpha^+$ puncta apposing $CB1R^+$

varicosities at the cell surface of postsynaptic IL- or PL-projecting PNs revealed a significantly higher number at PN_{IL} somata (Figures 4F–4H; PN_{IL}: 61.0 (44.0/76.8) spots per soma, n = 56, N = 4; PN_{PL}: 40.5 (32.5/58.0), n = 44, N = 3; MWU test $p < 0.001$). Consistent with our previous results obtained in naive animals, the number of $DGL\alpha^+$ puncta in IL-projecting PNs was circa 50% higher compared to PL-projecting PNs. Thus, the difference in DGLα abundance in distinct BA→mPFC output pathways reflects a fear learning-independent cellular property of defined BA PNs. Together, these findings indicate that, in the BA, behavioral specificity of projection pathways is regulated by postsynaptic differences in endocannabinoid signaling.

DISCUSSION

CB1R-expressing CCK_L INs have been proposed to be major regulators of fear extinction circuits (Marsicano et al., 2002) and emotional states (Freund, 2003). However, until recently, investigating their functional role was impeded by a lack of specific genetic tools. Using an intersectional genetic strategy, we were able to selectively label CCK-expressing basket cells with GFP. Although about 10% of GFP^+ CCK_Ls were not immunopositive for CCK, none of these cells displayed a pyramidal-like morphology, confirming that we specifically target interneurons with our intersectional strategy. Most likely, these neurons were not labeled by the CCK antibody due to very low somatic abundance of CCK peptide at the time of the experiment.

Using this mouse model, we were able to achieve targeted paired patch-clamp recordings of GFP-expressing CCK_Ls and defined subpopulations of retrogradely labeled BA PNs. This approach enabled us to study the cell-type-specific organization of CCK_L-mediated inhibitory synaptic transmission in fear and extinction micro-circuits of the mouse amygdala. We observed that CCK_Ls uniformly inhibit IL- and PL-projecting BA PNs with similar connectivity and synaptic strength. Furthermore, we did not discover any differences in CCK_L spiking properties targeting either postsynaptic cell type. These data suggest that CCK_Ls targeting mPFC-projecting PNs are a rather homogeneous population of INs and that asymmetries promoting fine-tuning of output pathways might not be present on the level of unitary connectivity. Yet, we cannot exclude that amygdala CCK_Ls, similar to $CB1R^+$/$VGlut3^+$ CCK INs in entorhinal cortex (Varga et al., 2010), could connect onto PNs projecting to brain regions other than mPFC in a target-specific manner. Also, as recently reported for hippocampal INs (Dudok et al., 2015), it is possible that amygdala CCK_Ls are heterogeneous on a molecular level, e.g., with regard to the subcellular distribution of CB1R protein.

In contrast to the unitary connectivity and synaptic strength, we found that the dynamics of CCK_L-mediated synaptic inhibition onto distinct subpopulations of BA PNs are cell type and pathway specific. Both short-term synaptic plasticity and DSI are different for BA neurons projecting to either IL or PL. $CCK_L \rightarrow PN_{IL}$ synapses exhibit depressing short-term plasticity dynamics in response to presynaptic high-frequency spike trains, as well as reliable and robust activity-dependent DSI. In contrast, $CCK_L \rightarrow PN_{PL}$ synapses show facilitating compound IPSCs and a significantly weaker DSI.

In line with the notion that PN_{IL}s and PN_{PL}s are contacted by a similar population of CCK_Ls, we found that $CCK_L \rightarrow PN_{IL}$ synapses and $CCK_L \rightarrow PN_{PL}$ synapses are equally suppressed in response to the application of an exogenous CB1R antagonist and that the content of the presynaptic endocannabinoid-degrading enzyme MGL is similar at $CCK_L \rightarrow PN_{IL}$ and $CCK_L \rightarrow PN_{PL}$ synapses. In contrast, the postsynaptic abundance of the endocannabinoid-synthesizing enzyme DGLα is significantly greater in PN_{IL}s compared to PN_{PL}s, suggesting that cell-type-specific differences in the postsynaptic endocannabinoid signaling machinery are an important factor determining the specificity of CB1R-mediated signaling in amygdala micro-circuits.

Possible mechanisms for this differential postsynaptic expression of DGLα in IL- and PL-projecting BA PNs remain elusive. One conceivable mechanism could involve neurotrophic factors, which allow for retrograde signaling over long distances from the axon to the soma and can influence synaptic plasticity, as well as transcriptional programs that define neuronal identities (Zweifel et al., 2005). In particular, brain-derived neurotrophic factor (BDNF) has been implicated in extinction learning and IL function (Bredy et al., 2007; Soliman et al., 2010) and is enriched in brain regions controlling fear behavior, including mPFC and the amygdala (Hill and Martinowich, 2016). Furthermore, BDNF has been shown to directly interact with the endocannabinoid signaling machinery at cortical synapses (Lemtiri-Chlieh and Levine, 2010).

As previously described, the balance of activity between IL- and PL-projecting BA PNs is an important regulator determining the efficiency and strength of fear extinction learning (Senn et al., 2014). A higher DGLα abundance in PN_{IL}s was not only observed in naive mice, but also after fear conditioning. This target-specific differential expression of endocannabinoid signaling enzymes reflects a stable property of BA micro-circuits even after fear learning, when PN_{PL}s, but not PN_{IL}s, display high activity and undergo cell-type-specific plasticity (Senn et al., 2014). However, we cannot exclude that other future experiences could alter the expression of DGLα in IL- or PL-projecting BA PNs.

In the light of our present results, it is possible that during extinction learning (Senn et al., 2014), when IL-projecting BA neurons are strongly activated, inhibitory input from CCK_Ls onto IL-projecting PNs could rapidly be suppressed by activity-dependent mechanisms, including short-term depression and DSI, which in turn would boost the output of PN_{IL}s and consequently enhance the contrast between the two functionally distinct mPFC-projecting pathways. CCK_L basket cells could control the activity of PNs by shunting inhibition or hyperpolarization, which could be released during burst excitation specifically within the BA-IL pathway during fear extinction training. So far, we do not know how CCK INs could influence the integration of excitatory stimuli in IL- or PL-projecting BA PNs. Future studies investigating the activity patterns and recruitment of CCK_Ls in vivo will be necessary to understand the temporal relation between CCK_Ls and PN firing during fear learning and extinction.

Together, the present data indicate that cell-type-specific, short-term synaptic plasticity may function as a general mechanism to transform uniform recruitment of CCK_Ls into asymmetric inhibitory input onto projection-specific subpopulations of PNs.

This projection-specific shift in the balance between inhibition and activity-dependent disinhibition could enhance the contrast between distinct output pathways to promote rapid behavioral adaptations.

EXPERIMENTAL PROCEDURES

Animals

Mice were group housed in a temperature-controlled room with a 12 hr light/dark cycle and unlimited access to food and water. All procedures were carried out with the approval of the Veterinary Department of the Canton Basel-Stadt.

CCK-IN-GFP transgenic mice were generated using an intersectional strategy. Mice expressing Flp under a pan-GABAergic promoter Dlx (*Dlx-Flp*) (Miyoshi et al., 2010) were crossed with *CCK-IRES-Cre* Cre-driver mice (Taniguchi et al., 2011). Subsequent crossing of *Dlx-Flp::CCK-IRES-Cre* offspring with the *RCE:dual* conditional reporter line (Taniguchi et al., 2011) yielded progeny with exclusive GFP expression in Cre^+/Flp^+ GABAergic, but not Cre^+/Flp^- glutamatergic CCK-expressing neurons. 4- to 10-week-old CCK-IN-GFP male mice were used for all electrophysiological experiments. For histology, 6- to 8-week-old male CCK-IN-GFP mice and age-matched wild-type (WT) littermates were used. For analysis of cell surface area of mPFC-projecting PNs, we used 8-week-old male hCar::tdTomato mice, which ubiquitously express the hCAR receptor (Tallone et al., 2001), crossed with the Ai9 tdTomato reporter line. Mice were single housed after surgical procedures.

Stereotactic Delivery of Retrograde Labels

Retrograde labeling of BA→mPFC-projecting neurons was carried out by IL/PL localized stereotactic injections of either red fluorophore-coated latex beads (Lumafluor) for electrophysiology or with Alexa 555-conjugated Choleratoxin-B (Life Technologies) or CAV2-cre virus for histology. Beads were dialyzed against 0.32 M sucrose solution on floating polycarbonate membrane filters (Steriltech; pore size 0.01 μm, diameter 25 mm). Mice were anesthetized with isoflurane (Minirad) in oxygen-enriched air (Oxymat 3, Weinmann) and placed in a stereotaxic frame (Kopf Instruments). Body temperature was maintained at 35.5°C with a feedback-controlled heating pad (FHC). Analgetics were delivered prior to surgical incision (meloxicam [60 μL of 0.5 mg/mL, intraperitoneally (i.p.), Metacam, Boehringer Ingelheim] and ropivacain [120 μL under the scalp, Naropin, AstraZeneca]). A picospritzer (Parker Hannifin Corporation) connected to a flame-pulled (P-97, Sutter Instruments) borosilicate micropipette (World Precision Instruments) was used to deliver retrobeads, Choleratoxin-B, or CAV2-cre virus (0.1 μL) bilaterally to mPFC subdivisions using the following coordinates (in mm from bregma): rostral + 1.85, lateral ± 0.35, ventral 2.2 (PL), or 2.75 (IL). Postsurgery treatment involved injection of meloxicam (60 μL of 0.5 mg/mL, i.p., Metacam) to reduce pain and inflammation risk. Animals were allowed to recover 10 days before perfusion for immunohistochemical analysis or 1–14 days before subsequent electrophysiological experiments. Average recovery times did not differ between IL- and PL-injected mice (for DSI experiments: IL: 4.8 ± 0.7 days, N = 14; PL: 6.3 ± 0.8 days, N = 21; t test $p > 0.05$). Average age of the mice at the time of electrophysiological experiments was about 6 weeks and was not different between IL- and PL-injected mice (for DSI experiments: IL: 41.8 ± 2.4 days, N = 14; PL: 44.0 ± 2.1 days, N = 21; t test $p > 0.05$).

Electrophysiology

Mice were deeply anesthetized with 5% isoflurane and decapitated. Brains were dissected in ice-cold artificial cerebrospinal fluid (aCSF) containing (in mM) 124 NaCl, 2.7 KCl, 2 $CaCl_2$, 1.3 $MgCl_2$, 26 $NaHCO_3$, 0.4 NaH_2PO_4, 18 glucose, and 2.25 ascorbate, equilibrated with 95% O_2/5% CO_2. Coronal slices (300 μm thickness) were cut with a vibratome (Microm HM 650 V) with sapphire blades (Delaware Diamond Knives), stored in an interface chamber, and recovered for 45 min at 37°C. Whole-cell patch-clamp recordings from CCK INs and IL/PL-projecting PN pairs/triples (max. 350 μm apart) were carried out at 32°C under constant perfusion with 95% O_2/5% CO_2-equilibrated aCSF. GFP^+ and bead-labeled neurons were identified under an upright microscope (Olympus BX50WI) fitted with epifluorescence and infrared optics (EM-CCD Camera, Hamamatsu). Borosilicate glass (GC150T-7.5, Harvard Apparatus) was used to pull patch electrodes (DMC Universal Puller, Zeitz Instruments GmbH) with a resistance of 3–4 MΩ. Intracellular recording solution contained (in mM): 106 K-Methylsulfate, 40 KCl, 20 Na-Phosphocreatine, 0.3 Na-GTP, 4 Mg-ATP, and 10 HEPES. Osmolarity was adjusted to 280–290 mOsm and pH to 7.2–7.25. Electrophysiological recordings were acquired (Multiclamp 700B, Molecular Devices), sampled at 50 kHz, filtered at 4 kHz (voltage clamp) or 10 kHz (current clamp; Digidata 1440 A, pClamp 10; Molecular Devices), and analyzed offline with Clampfit (Molecular Devices) and Igor Pro (Wavemetrics). Access resistance was monitored throughout experiments by injection of 5 mV hyperpolarizing current steps. When access resistance increased more than 20%, the protocol was terminated. To evoke action potentials in CCK_Ls, we injected 1,200 pA currents steps of 2 ms duration. For stimulating PNs, the pulse duration was increased to 4 ms. Connectivity was assessed by analysis of IPSCs in response to presynaptic bursts at 100 Hz for a duration of 50 ms every 10 s. At least ten traces were recorded and averaged for each pair. For DSI protocols, 20 Hz trains of eight action potentials were elicited in CCK_Ls every 10 s. Due to variability in IPSC amplitude and occasional failures, the amplitude of postsynaptic responses to the presynaptic spike train was averaged in each trace. DSI was induced by depolarizing PNs to 0 mV for 5 s. Physiological DSI was elicited by applying an action potential train with Poisson distribution for 5 s (mean frequency: 100 Hz, range: 30–250 Hz). During pharmacological experiments, CCK_Ls were stimulated every 10 s with two action potentials of 50 ms inter-spike interval followed by a 500 ms break and five action potentials with 12.5 ms inter-spike interval. Spiking patterns were assessed by applying 40 current steps from −140 pA to 260 pA.

Behavior

Nine days after choleratoxin-B injection to mPFC subdivisions, mice were submitted to an auditory fear conditioning paradigm. Five pairings of auditory conditioned stimulus (CS) and aversive unconditioned stimulus (US) were presented with an intertrial interval of 78–110 s. The CS consisted of 50 ms pips repeated at 0.9 Hz (total duration of 30 s) with a pip frequency of 7.5 kHz and 75 dB sound pressure level (Tucker-Davis Technologies) and was followed by a 1 s 0.65 mA AC foot shock (Coulbourn Instruments). Freezing behavior was classified as a 2 s absence of movement and quantified using Cineplex Studio and CinePlex Editor video tracking software (Plexon) and custom-written MATLAB (MathWorks) routines. Mice were perfused for immunohistochemical analysis 24 hr after fear conditioning.

Immunohistochemistry

Mice were anesthetized with 3% isoflurane followed by an injection of urethane (2.5 g/kg, i.p.). Animals were perfused with cold 4% paraformaldehyde in phosphate buffer (pH 7.4; 100 mL/animal) following an injection of 300 U heparin to the left ventricle. After 2 hr postfixation, coronal brain sections (60 μm) were prepared with a vibratome (Leica Microsystems) and stored in PBS. Working solutions contained 0.5% Triton in PBS (PBST) and normal goat serum (NGS). Free-floating sections were washed with PBS three times before treatment with blocking solution (10% NGS in PBST, 2 hr at room temperature) and incubated at 4°C for 48 hr with a combination of the following primary antibodies in 1% NGS in PBST: chicken anti-GFP (1:1,000; Invitrogen), rabbit anti-CCK (1:500; Frontiers Institute), guinea pig anti-PV (1:500; Synaptic Systems), rat anti-SOM (1:500; Millipore), mouse and rabbit anti-VGAT (1:300; Synaptic Systems), guinea pig anti-CB1R (1:500; Frontiers Institute), rabbit anti-DGLα (1:500; Frontiers Institute), rabbit anti-MGL (1:500; Frontiers Institute), and mouse anti-gephyrin (1:500, Synaptic Systems). Sections were washed with PBS three times before secondary antibody incubation (1% NGS in PBST, 24 hr at 4°C) with a combination of the following antibodies: goat anti-mouse DyLight 405 (1:500; Thermo Scientific), goat anti-guinea pig DyLight 405 (1:250; Jackson ImmunoResearch), goat anti-mouse Alexa 488, goat anti-rabbit Alexa 405, goat anti-rabbit Alexa 488, goat anti-rabbit Alexa 647, goat anti-chicken Alexa 488, goat anti-guinea pig Alexa 647, goat anti-rat Alexa 647, and goat anti-rat Alexa 568 (all 1:1,000; Thermo Scientific). Sections were rinsed four times with PBS, mounted, and coverslipped on glass slides. Sections containing retrogradely labeled IL- and PL-projecting cells for quantitative analysis of endocannabinoid signaling-protein expression were always processed in parallel with the same working solutions.

Confocal Microscopy and Image Analysis

Confocal images were acquired using a LSM 700 microscope (Carl Zeiss) equipped with four laser lines (405, 488, 555, and 639 nm). For analysis of GFP^+ IN and PN cell size, as well as for basic characterization of molecular marker expression of GFP^+ INs, z sections (3 μm) of the BA of CCK-IN-GFP and hCar::tdTomato mice were scanned with a 20× objective (Plan-Apochromat 20×/0.8, Zeiss). Every third of quadruple-labeled sections containing the BA were scanned and analyzed unilaterally for quantification of molecular marker expression. GFP^+ INs were considered as CCK_L if their somatic surface area was within one SD of the somatic surface area of mPFC-projecting BA PNs. Z stacks for analysis of CB1R, DGLα, MGL, VGAT, and gephyrin subcellular localization were acquired at 63× magnification (Plan-Apochromat 63×/1.40 Oil DIC objective, Zeiss) with 1.3-fold digital zoom, a pixel size of 80 nm, image size of 1,024 × 1,024 pixels, pinhole 1 airy unit, and 200 nm z-steps. Different channels of triple- or quadruple-labeled sections were scanned sequentially as frames with a pixel time of 0.79 μs. Photomultiplier settings were individually adjusted for sampling over the full dynamic range, and images were averaged twice to optimize signal-to-noise ratio. mPFC-projecting cells were scanned over the whole rostro-caudal extend of the BA. Images were deconvolved using Huygens Software (Scientific Volume Imaging). Quantification was performed manually in a blind manner in deconvolved 3D images using Imaris software (Bitplane AG). Background noise was eliminated by baseline subtraction (5%). $CB1R^+$ terminals from CCK interneurons were formed as elongated varicosities with an approximate diameter of 1–2 μm around PN cell bodies. GABAergic identity was confirmed by co-immunolabelling with VGAT. Terminals containing one or more VGAT-positive spots (diameter approximately 0.5–1 μm) were scored if the VGAT signal was covered by at least 90% with the CB1R signal. The same criterion was applied for MGL analysis. For DGLα and gephyrin, only puncta with round or oval morphology and a diameter of approximately 0.3–0.5 μm were scored. Immunofluorescent signals of CB1R and DGLα were distributed in a mutually exclusive manner but closely apposed to one another at the cellular membrane. DGLα was considered to be colocalized with gephyrin if at least 25% of its area was covered by the gephyrin signal. All focal planes of uncut cell bodies were analyzed. Cellular surface area was determined using the MeasurementsPro Plugin of Imaris software. Brightness and contrast of example images were adjusted with ImageJ.

Statistical Analyses

All datasets were tested for Gaussian distribution using a one-sample Kolmogorov-Smirnov test. In case that the null hypothesis of normal distribution was not rejected, two groups were statistically compared using a Student's t test, and the data values are expressed as mean ± SEM. Welch's correction was applied in case of unequal variances. If the null hypothesis of normal distribution was rejected, two datasets were compared using a Mann-Whitney U (MWU) test and are presented as median values and $25^{th}/75^{th}$ percentiles. Figures additionally display 10^{th} to 90^{th} percentiles. Paired datasets were analyzed with a Wilcoxon matched-pairs signed-rank test. A two-way ANOVA was applied when comparing two groups for multiple time points and combined with a Bonferroni post hoc test (null hypothesis of normal distribution was not rejected). Connectivity ratios were matched using Fisher's exact test. To compare cumulative distributions between two groups, we applied a two-sample Kolmogorov-Smirnov test. The number of analyzed cells is indicated with "n," while "N" declares the number of animals from which these cells were obtained. Statistical significance levels are presented as $*p < 0.05$, $**p < 0.01$, or $***p < 0.001$ in all figures. Statistical analysis was carried out with Prism 6 (GraphPad Software) and Microsoft Excel (Microsoft Corporation).

SUPPLEMENTAL INFORMATION

Supplemental Information includes four figures and three tables and can be found with this article online at http://dx.doi.org/10.1016/j.neuron.2016.06.036.

AUTHOR CONTRIBUTIONS

E.V., S.K., J.G., and A.L. designed the experiments. E.V., S.K., and J.G. performed the experiments and analyzed the data. E.V., S.K., J.G., J.I.W.C., and A.L. wrote the paper. All authors approved the final version of the manuscript.

ACKNOWLEDGMENTS

We would like to thank T. Klausberger and all members of the Lüthi lab for discussions and critical comments on the manuscript; Christian Müller, Kristine Bylund, and Tingjia Lu for excellent technical assistance; the FMI microscopy facility for support with image acquisition and analysis; and J. Huang, G. Fishell, S. Arber, and S. Pettersson for providing mouse lines. This work was supported by the Novartis Research Foundation, by an ERC Advanced Grant, by the National Center of Competences in Research: "SYNAPSY - The Synaptic Bases of Mental Diseases" (financed by the Swiss National Science Foundation), by an SNSF core grant (to A.L.); and by fellowships from EMBO and the Swiss National Science Foundation, Ambizione (to J.G.); EMBO and the Canadian Institutes for Health Research (to J.I.W.C.); and a Young Investigator Grant from the Brain & Behaviour Research Foundation (to S.K.).

Received: March 5, 2015
Revised: May 2, 2016
Accepted: June 22, 2016
Published: August 3, 2016

REFERENCES

Armstrong, C., and Soltesz, I. (2012). Basket cell dichotomy in microcircuit function. J. Physiol. *590*, 683–694.

Bock, D.D., Lee, W.C., Kerlin, A.M., Andermann, M.L., Hood, G., Wetzel, A.W., Yurgenson, S., Soucy, E.R., Kim, H.S., and Reid, R.C. (2011). Network anatomy and in vivo physiology of visual cortical neurons. Nature *471*, 177–182.

Bredy, T.W., Wu, H., Crego, C., Zellhoefer, J., Sun, Y.E., and Barad, M. (2007). Histone modifications around individual BDNF gene promoters in prefrontal cortex are associated with extinction of conditioned fear. Learn. Mem. *14*, 268–276.

Brown, S.P., and Hestrin, S. (2009). Intracortical circuits of pyramidal neurons reflect their long-range axonal targets. Nature *457*, 1133–1136.

Burgos-Robles, A., Vidal-Gonzalez, I., and Quirk, G.J. (2009). Sustained conditioned responses in prelimbic prefrontal neurons are correlated with fear expression and extinction failure. J. Neurosci. *29*, 8474–8482.

Dudok, B., Barna, L., Ledri, M., Szabó, S.I., Szabadits, E., Pintér, B., Woodhams, S.G., Henstridge, C.M., Balla, G.Y., Nyilas, R., et al. (2015). Cell-specific STORM super-resolution imaging reveals nanoscale organization of cannabinoid signaling. Nat. Neurosci. *18*, 75–86.

Freund, T.F. (2003). Interneuron Diversity series: Rhythm and mood in perisomatic inhibition. Trends Neurosci. *26*, 489–495.

Galarreta, M., Erdélyi, F., Szabó, G., and Hestrin, S. (2004). Electrical coupling among irregular-spiking GABAergic interneurons expressing cannabinoid receptors. J. Neurosci. *24*, 9770–9778.

Harris, K.D., and Mrsic-Flogel, T.D. (2013). Cortical connectivity and sensory coding. Nature *503*, 51–58.

Hashimotodani, Y., Ohno-Shosaku, T., Maejima, T., Fukami, K., and Kano, M. (2008). Pharmacological evidence for the involvement of diacylglycerol lipase in depolarization-induced endocanabinoid release. Neuropharmacology *54*, 58–67.

Hefft, S., and Jonas, P. (2005). Asynchronous GABA release generates long-lasting inhibition at a hippocampal interneuron-principal neuron synapse. Nat. Neurosci. *8*, 1319–1328.

Hill, J.L., and Martinowich, K. (2016). Activity-dependent signaling: influence on plasticity in circuits controlling fear-related behavior. Curr. Opin. Neurobiol. *36*, 59–65.

Hofer, S.B., Ko, H., Pichler, B., Vogelstein, J., Ros, H., Zeng, H., Lein, E., Lesica, N.A., and Mrsic-Flogel, T.D. (2011). Differential connectivity and

response dynamics of excitatory and inhibitory neurons in visual cortex. Nat. Neurosci. *14*, 1045–1052.

Hoover, W.B., and Vertes, R.P. (2007). Anatomical analysis of afferent projections to the medial prefrontal cortex in the rat. Brain Struct. Funct. *212*, 149–179.

Katona, I., Rancz, E.A., Acsady, L., Ledent, C., Mackie, K., Hajos, N., and Freund, T.F. (2001). Distribution of CB1 cannabinoid receptors in the amygdala and their role in the control of GABAergic transmission. J. Neurosci. *21*, 9506–9518.

Le Bé, J.V., and Markram, H. (2006). Spontaneous and evoked synaptic rewiring in the neonatal neocortex. Proc. Natl. Acad. Sci. USA *103*, 13214–13219.

Lemtiri-Chlieh, F., and Levine, E.S. (2010). BDNF evokes release of endogenous cannabinoids at layer 2/3 inhibitory synapses in the neocortex. J. Neurophysiol. *104*, 1923–1932.

Liu, B.H., Li, P., Sun, Y.J., Li, Y.T., Zhang, L.I., and Tao, H.W. (2010). Intervening inhibition underlies simple-cell receptive field structure in visual cortex. Nat. Neurosci. *13*, 89–96.

Marsicano, G., Wotjak, C.T., Azad, S.C., Bisogno, T., Rammes, G., Cascio, M.G., Hermann, H., Tang, J., Hofmann, C., Zieglgänsberger, W., et al. (2002). The endogenous cannabinoid system controls extinction of aversive memories. Nature *418*, 530–534.

Mascagni, F., and McDonald, A.J. (2003). Immunohistochemical characterization of cholecystokinin containing neurons in the rat basolateral amygdala. Brain Res. *976*, 171–184.

Miyoshi, G., Hjerling-Leffler, J., Karayannis, T., Sousa, V.H., Butt, S.J., Battiste, J., Johnson, J.E., Machold, R.P., and Fishell, G. (2010). Genetic fate mapping reveals that the caudal ganglionic eminence produces a large and diverse population of superficial cortical interneurons. J. Neurosci. *30*, 1582–1594.

Ohno-Shosaku, T., Maejima, T., and Kano, M. (2001). Endogenous cannabinoids mediate retrograde signals from depolarized postsynaptic neurons to presynaptic terminals. Neuron *29*, 729–738.

Quirk, G.J., and Mueller, D. (2008). Neural mechanisms of extinction learning and retrieval. Neuropsychopharmacology *33*, 56–72.

Sassoè-Pognetto, M., Panzanelli, P., Sieghart, W., and Fritschy, J.M. (2000). Colocalization of multiple GABA(A) receptor subtypes with gephyrin at postsynaptic sites. J. Comp. Neurol. *420*, 481–498.

Senn, V., Wolff, S.B., Herry, C., Grenier, F., Ehrlich, I., Gründemann, J., Fadok, J.P., Müller, C., Letzkus, J.J., and Lüthi, A. (2014). Long-range connectivity defines behavioral specificity of amygdala neurons. Neuron *81*, 428–437.

Sierra-Mercado, D., Padilla-Coreano, N., and Quirk, G.J. (2011). Dissociable roles of prelimbic and infralimbic cortices, ventral hippocampus, and basolateral amygdala in the expression and extinction of conditioned fear. Neuropsychopharmacology *36*, 529–538.

Soliman, F., Glatt, C.E., Bath, K.G., Levita, L., Jones, R.M., Pattwell, S.S., Jing, D., Tottenham, N., Amso, D., Somerville, L.H., et al. (2010). A genetic variant BDNF polymorphism alters extinction learning in both mouse and human. Science *327*, 863–866.

Tallone, T., Malin, S., Samuelsson, A., Wilbertz, J., Miyahara, M., Okamoto, K., Poellinger, L., Philipson, L., and Pettersson, S. (2001). A mouse model for adenovirus gene delivery. Proc. Natl. Acad. Sci. USA *98*, 7910–7915.

Taniguchi, H., He, M., Wu, P., Kim, S., Paik, R., Sugino, K., Kvitsiani, D., Fu, Y., Lu, J., Lin, Y., et al. (2011). A resource of Cre driver lines for genetic targeting of GABAergic neurons in cerebral cortex. Neuron *71*, 995–1013.

Tanimura, A., Yamazaki, M., Hashimotodani, Y., Uchigashima, M., Kawata, S., Abe, M., Kita, Y., Hashimoto, K., Shimizu, T., Watanabe, M., et al. (2010). The endocannabinoid 2-arachidonoylglycerol produced by diacylglycerol lipase alpha mediates retrograde suppression of synaptic transmission. Neuron *65*, 320–327.

Trouche, S., Sasaki, J.M., Tu, T., and Reijmers, L.G. (2013). Fear extinction causes target-specific remodeling of perisomatic inhibitory synapses. Neuron *80*, 1054–1065.

Varga, C., Lee, S.Y., and Soltesz, I. (2010). Target-selective GABAergic control of entorhinal cortex output. Nat. Neurosci. *13*, 822–824.

Wehr, M., and Zador, A.M. (2003). Balanced inhibition underlies tuning and sharpens spike timing in auditory cortex. Nature *426*, 442–446.

Wilson, R.I., and Nicoll, R.A. (2001). Endogenous cannabinoids mediate retrograde signalling at hippocampal synapses. Nature *410*, 588–592.

Wilson, R.I., and Nicoll, R.A. (2002). Endocannabinoid signaling in the brain. Science *296*, 678–682.

Wilson, R.I., Kunos, G., and Nicoll, R.A. (2001). Presynaptic specificity of endocannabinoid signaling in the hippocampus. Neuron *31*, 453–462.

Zweifel, L.S., Kuruvilla, R., and Ginty, D.D. (2005). Functions and mechanisms of retrograde neurotrophin signalling. Nat. Rev. Neurosci. *6*, 615–625.